

Evolution of a shock-accelerated thin fluid layer

P. M. Rightley,^{a)} P. Vorobieff, and R. F. Benjamin
Los Alamos National Laboratory, Los Alamos, New Mexico 87545

(Received 11 November 1996; accepted 3 February 1997)

Multi-exposure flow visualization experiments with laser-sheet illumination provide growth-rate measurement of Richtmyer–Meshkov instability of a thin, perturbed heavy-gas layer embedded in a lower-density gas and accelerated by a planar shock wave. The measurements clearly show the three-stage transition to turbulence of this gas-curtain instability and the single-event coexistence of the three primary flow morphologies discovered previously. The shock-induced circulation for each event is estimated using a simple model based on Richtmyer–Meshkov instability and an infinite linear array of vortex points. These estimates are consistent with simplified flow simulations using a finite-core vortex-blob model. [S1070-6631(97)01206-3]

I. INTRODUCTION

Experimental measurements of the growth rate of a thin, heavy fluid layer accelerated by a shock wave lead to better understanding of Richtmyer–Meshkov (RM) instability (Richtmyer,¹ Meshkov²), the impulsively driven analog of the well-known Rayleigh–Taylor instability. The multi-exposure flow visualization presented in this study shows the same basic flow patterns that were previously observed (Jacobs *et al.*,^{3,4} Budzinski *et al.*⁵), but now we also observe the coexistence of flow patterns not recorded in previous experiments. Analysis of these images using simple, analytic models shows remarkable similarity of the observations with flows induced by a row of vortices alternating in sign. These models and new data sets enable estimation of the vorticity produced by the interaction of a shock wave with closely spaced rippled interfaces from visual information only (i.e., without direct measurement of velocity fields).

The recent experiments improve the understanding of the instability phenomena limiting the efficacy of inertial confinement fusion targets (McCall⁶), and involving subjects in astrophysics (Burrows *et al.*⁷ and Stone *et al.*⁸). Studies of Rayleigh–Taylor instability in the presence of magnetic fields and variable deceleration are important for the understanding of the evolution of supernovas (Jun and Jones⁹). In addition to providing new insights about fluid instability, the present results are useful as benchmarks for code development involving fluid simulations.

The thin fluid layer of heavy gas is embedded between fluids of lower density by the laminar flow of the heavy gas vertically downward through the lighter gas. This initial heavy-gas flow constitutes the thin fluid layer, and is denoted a “gas curtain.” The gas curtain has imposed perturbations on both upstream and downstream interfaces. A planar shock wave enters the test region in the lower-density fluid (air), passes through the gas curtain composed of SF₆ gas traced with fog, then exits the test region in the lower-density fluid (air) on the downstream side. Under the impulsive acceleration of the shock wave, both upstream and downstream interfaces are Richtmyer–Meshkov unstable and consequently distort as the layer moves downstream. At the upstream interface the shock front moves from lower-density gas into

higher-density gas, so the interfacial ripples grow immediately after shock compression. At the downstream interface, the shock front moves from higher-density gas into lower-density gas, so the interfacial perturbations must first reverse phase and then grow. The visual result for the entire layer is that the initially varicose perturbation of the gas curtain becomes sinuous and later mushroom-shaped or plume-shaped. However, asymmetries in the perturbed gas curtain dramatically hasten the onset of mushroom shapes. Thus, three basic flow patterns are observed: upstream-facing mushrooms, downstream-facing mushrooms and sinuous pattern. Each experiment produces one or a combination of two or three of these patterns.

Previous experimental studies (Jacobs *et al.*^{3,4}) of the gas curtain evolution revealed these three distinct flow patterns. Subsequent experiments (Budzinski *et al.*⁵) showed correlation of the evolving flow pattern with the initial configuration of the gas curtain. For example, when perturbations on the upstream side of the curtain have amplitudes much larger than those on the downstream side, the resulting flow usually produces upstream-facing mushrooms. These earlier studies captured only one or two frames per event because they required high-energy lasers (0.2–1 J per pulse), and therefore detailed instability growth rates could not be measured. However, a computational study of these data by Baltrusaitis *et al.*¹⁰ did show the progression of the instability growth. By capturing a series of images for each event, our observations show the nonlinear growth of the instability, which eventually leads to interfacial mixing and turbulence. Our focus in this study is the nonlinear instability growth, but our results also provide qualitative information on the issue of “ordered versus disordered turbulence,” that is considered in recent theoretical^{11,12} and experimental^{13,14} studies of the transition to turbulence.

Most of the experiments show three temporal intervals in the flow, as one can see in the figures of Section III. We show that the first interval is dominated by shock-induced vorticity that controls the flow of the gas curtain beginning to penetrate the surrounding air masses. The flow is largely deterministic and appears to be governed by a linear array of vortices of alternating sign. The dominant wavelength is that of the initial perturbation. Differences between the flow morphologies are subtle.

In the second interval, the streamwise amplitude of the

^{a)}Corresponding author. Telephone: (505) 667-0460; Fax: (505) 665-3359; Electronic mail: pright@lanl.gov

curtain grows substantially. The spatial spectrum at wavelengths shorter than the 6 mm fundamental wavelength of the initial layer also exhibits growth. Most of the growth is deterministic, well-described by vortex-induced flow models, but spatial features in some of the data sets appear to be stochastic. The difference between the flow morphologies becomes apparent within this interval. Thus the second time interval corresponds to “ordered turbulence,”¹¹ meaning that the spectrum of the flow is evolving toward a fully developed turbulent spectrum, but the appearance of the flow remains deterministic. Another perception (Cranfill¹²) is that the spanwise velocity components of the flow near the “mushroom caps” indicate the onset of disorder. Visually, each mushroom or sinusoid structure seems to grow independently from each other.

Finally, the third interval is characterized by more complex flow patterns. Spatial structures interact with each other, producing spectra at wavelengths longer than the fundamental. Simultaneously, shorter-wavelength features grow markedly, and these features are predominantly stochastic. Interaction of large-scale vortex structures can produce shear, leading to Kelvin–Helmholtz instability. This instability and other phenomena result in formation of smaller-scale vortices. The third interval corresponds to “disordered turbulence,” and to the conventional perception of turbulence as a disordered state.

The progression of a flow through these three temporal intervals has also been observed in unstable flows other than Richtmyer–Meshkov instability of a gas curtain. These intervals are apparent in the images of Snider and Andrews,¹³ corresponding to Rayleigh–Taylor instability. The Kelvin–Helmholtz instability of free shear layers displays similar behavior in the creation of streamwise vortices superimposed upon the large spanwise coherent structures and the eventual increase of energy in small-scale random motions. In combination with the pairing mechanism of the streamwise structures, this results in the energy spectrum increasing for both larger and smaller wave numbers than that of the initial roll-up.¹⁴

The streamwise position of the shock-induced vortices relative to the gas curtain influences the subsequent flow evolution. Consider an inviscid, incompressible, constant-density flow induced by a linear array of vortices of alternating sign. Although this model does not account for such important features of the real flow as density gradients, by using massless marker particles for visualization and varying the initial position of the markers with respect to the array, we produce simulated patterns similar to those in the experimental images.

Our multi-exposure diagnostic method is a considerable improvement over earlier experiments with laser-induced fluorescence and Rayleigh scattering directly from the SF_6 . Tracer fog added to the SF_6 in the gas curtain enhances the light scattering from the layer, which reduces the laser energy requirements enormously. We routinely acquire 8–10 dynamic images (in addition to the image of the initial condition), and most images have better spatial resolution than the earlier data. Evidence for the fog being a suitable flow tracer is presented in the next section.

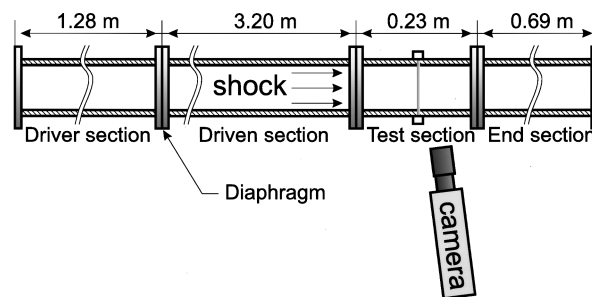


FIG. 1. Schematic of the experimental facility.

The images obtained by laser-sheet illumination of the thin layer provide a relative measure of the density distribution within a two-dimensional slice of the flow. The tracer provides adequate definition to measure the mixing width although it precludes the quantitative measure of layer density that is possible with Rayleigh scattering directly from SF_6 molecules.

Computational studies of gas-curtain instability by Baltrusaitis *et al.*¹⁰ and Mikaelian¹⁵ show how each of the three families of flow patterns is produced, and the dependence of these patterns on initial conditions. The work of Baltrusaitis *et al.*¹⁰ did use experimentally measured initial conditions to benchmark their fluid dynamical algorithm, but did not consider the exact initial conditions producing the combination of patterns found here. Earlier work by Grove¹⁶ showed good agreement between computation and experimental results for a single, RM unstable interface between gases of different densities, and demonstrated the need to measure growth rates to discriminate among theories.

The next section provides details of the experimental setup, particularly the fog generator. Section III shows observed images and Section IV presents analysis of these images using a simple vortex model that incorporates the analytic description of Richtmyer–Meshkov instability for producing vorticity. Section IV also describes results obtained from simulations using a simple vortex-blob model of a flow driven by a linear array of vortices. We compare the model and experimental data with several combinations of fitting parameters, and find consistent estimates for the shock-induced circulation.

II. EXPERIMENTAL DETAILS

A. Experimental facility

A thin curtain of SF_6 embedded in air is shock-accelerated within a 5.5 m horizontal shock tube with internal dimensions of 75 mm square (Fig. 1). The facility and procedures are similar to those described by Jacobs *et al.*⁴ A Mach 1.2 shock is generated by breaking a diaphragm composed of two or three thin sheets of polypropylene separating a driver section pressurized to a gauge pressure of approximately 140 kPa from the driven section initially at ambient pressure. The progress of the shock wave through the test section causes an impulsive acceleration of the curtain. The optical diagnostic system must be triggered by the shock wave because the solenoid-actuated cutter produces a large

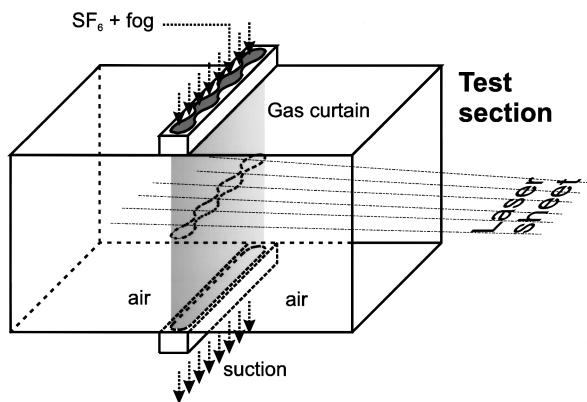


FIG. 2. Schematic of the test section.

time jitter between the system trigger and the shock impact on the gas curtain. Three piezoelectric flush-mounted pressure transducers are located on the wall of the driven section. The first two transducers characterize the shock velocity and pressure jump, and this information is later used to determine the “quality” of the shock (i.e. consistent speed for given pressure jump and the presence of a single shock front). The third transducer, which is closest to the test section, triggers the laser and camera.

A curtain of SF_6 gas embedded in the air (at ambient pressure) occupying the shock tube is generated within the test section (Fig. 2). The curtain has a cross-section of varicose shape, imposed by the nozzle through which SF_6 flows into the section. This nozzle at the top spans the entire 75 mm width of the section. The nozzle is fabricated with 4.76 mm diameter holes spaced 5.95 mm apart center-to-center. The holes are connected by a 2.38 mm wide slot. A 10×75 mm exhaust slot at the bottom of the section is attached to a suction system. Both the curtain material (SF_6 with fog) and the air entrained by the curtain are evacuated through this slot after the curtain material has passed over the vertical extent of the test section. The constant pressure in the tube is maintained by two ports (one far upstream of the test section and one far downstream) allowing replenishment air to enter the tube. This make-up air minimizes the shear instability along the SF_6 /air interfaces. The flow rates of make-up air were not measured quantitatively, but visual observation indicates that they remain low and the curtain stays laminar everywhere. The velocity of the curtain gas [$\mathcal{O}(10 \text{ cm/s})$] is very small compared to both the shock velocity [$\mathcal{O}(100 \text{ m/s})$] and the instability growth rates [$\mathcal{O}(10 \text{ m/s})$] and therefore should have no significant influence on the instability behavior.

The curtain is composed of SF_6 mixed with a small quantity of microscopic water/glycol droplets (fog), produced by a modified theatrical fog generator.¹⁷ Inside the fog generator, pressurized SF_6 moves through a heating chamber after entraining small quantities of fog fluid. The fluid flashes to steam which forms into droplets upon entering a radiator heat exchanger. No measurement of the mean droplet size was performed for this study, however, characterizations of the output of theatrical fog generators¹⁸ have found sizes on the order of $0.5 \text{ } \mu\text{m}$. The resultant fog of small, efficient

scatterers is entrained in the SF_6 gas entering the nozzle. The mixture entering the test section is a cool, nearly incompressible, white fog composed of very small droplets where the presence of glycol greatly increases the droplet lifetimes.

B. Diagnostics

The principal diagnostic is Rayleigh scattering from fog in the curtain illuminated by a horizontal laser sheet. The camera collects the light scattered from the curtain at approximately a 90° angle (Fig. 1). The slight camera tilt is necessitated by the curtain exhaust port obscuring the view of the curtain prior to shock impact. In this way, the curtain’s initial conditions can be imaged with only slight loss of downstream field-of-view. The enhanced Rayleigh scattering from the fog particles, compared to the scattering by the SF_6 alone (see Budzinski *et al.*⁵), allows multiple images to be obtained for each event. Due to the layer’s relative thinness and its mean motion downstream at the piston velocity of the shock, it is possible to lay multiple exposures on a single CCD camera array during the course of a single event. This eliminates the necessity of an expensive multi-framing high-speed camera. Two techniques can be applied to obtain time resolution of the resulting exposures.

In the first method, an intensified, gated CCD camera (Hadland Photonics SVR) is used in conjunction with a 1 W Ar^+ CW laser (Lexcel Model 94). Each of the nine exposures on the CCD is $2 \text{ } \mu\text{s}$ in duration, and produces excellent image quality at $2 \text{ } \mu\text{J}$ of optical energy. The camera uses two back-to-back Gen-1 intensifiers and provides the full CCD resolution of 1134×437 with 8 bits per pixel, corresponding to the physical image area size of $121.5 \times 46.8 \text{ mm}$. In a typical image, about 120 levels of brightness are actually present, with pixel values varying in the range between 30 and 150. This is considerably greater than the dynamic range of data from earlier studies.⁵ The direction of the shock wave propagation and the subsequent motion of the accelerated curtain in the photographs is from left to right, with the first image (exposure) of the SF_6 layer on the left showing its initial condition before interaction with the shock wave. All the consecutive images depict the time evolution of the layer after the interaction. This arrangement allows for arbitrary inter-exposure timings with a prescribed smallest-allowable timing derived from the thickness of the unstable layer and the mean downstream velocity. This requirement imposes greater and greater minimum inter-exposure timings to avoid overlapping images as the mixing width grows. For the images analyzed in this paper, the timing for the initial conditions is roughly $50 \text{ } \mu\text{s}$ prior to shock impact (although the time jitter for that event is estimated to be approximately $\pm 10 \text{ } \mu\text{s}$). The first dynamic image is approximately $60\text{--}70 \text{ } \mu\text{s}$ after shock acceleration, depending on the jitter, while the remaining exposures occur at intervals of 60, 80, 80, 120, 120, 120 μs , respectively.

The combination of the enhanced scattering from the fog droplets and the intensified camera generates higher signal-to-noise ratios with only about 10^{-5} of the effective light pulse energy of the study by Budzinski *et al.*⁵ Also, the ability to utilize arbitrary inter-exposure timings provides a

much larger amount of data for each event than using a fixed inter-exposure timing, as stated by Rightley and Benjamin.¹⁹

An unintensified and thermoelectrically cooled camera (Photometrics) is used in the second technique, deriving temporal resolution from a pulsed laser (Positive Light Merlin Nd:YLF). This method ensures the entire dynamic range of the camera is used—10 bits per pixel with a 512×512 resolution. In this arrangement the primary limitation is control of the intervals between exposures because of the fixed pulse repetition rate of the laser. The laser produces 15 W equivalent continuous power while pulsing at 5 kHz, which gives excellent image quality at 3 mJ of optical energy. From these images it is seen that the addition of the fog enables higher signal-to-noise ratios with at least two orders of magnitude less light without an intensifier than when using the scattering from SF₆ alone.

C. Flow-tracking fidelity

The addition of a particulate cloud to the gas curtain to increase its light scattering efficiency necessitates an investigation as to whether the individual particles follow fluid elements in this shock-accelerated system. The requirements of enhancing the system's light scattering characteristics and ensuring that the particles accurately follow all scales of the flow are in conflict. Light scattering efficiency increases with the droplet diameter d_p (especially as that moves into the Mie scattering regime, i.e. $d_p/\lambda \gg 1$, where λ is the wavelength of light), however, the inertia of the droplet increases with the cube of the diameter, making it less and less able to follow high-frequency fluctuations of the gas in which it is embedded.

The equation of motion for a heavy, spherical particle embedded in a lighter carrier phase can be written as

$$\rho_p \frac{\pi}{6} d_p^3 \frac{d\mathbf{u}_p}{dt} = -3\pi d_p \mu_g (\mathbf{u}_p - \mathbf{u}_g) \quad (1)$$

(i.e. inertia balances Stokes drag) where the subscript g denotes the gas carrier phase and p the dispersed (particle) phase, ρ denotes density, \mathbf{u} velocity and μ the absolute viscosity. Terms including buoyancy, the influence of the dynamic pressure field and added mass are insignificant here (i.e. in the case of heavy particles embedded in a lighter carrier).

A simplified description of the acceleration of the fog particles is that of the passage of a single shock and a resultant acceleration to the shock piston velocity. Integration of Eq. (1) for a particle at rest exposed to the shock piston velocity for this study (≈ 100 m/s) indicates that a relaxation time to achieve 99% of the piston velocity is approximately 3 μ s for a 0.5 μ m particle. This suggests that the fog particles will lag the SF₆ fluid particles by approximately 0.3 mm. The effective blur due to non-ideal particle tracking is on the order of three pixel sizes, thus limiting the spatial resolution of this study.

However, the shock interaction with the gas curtain is more complex than a single shock passage.⁴ A series of shock reflections and refractions from the two density interfaces occurs prior to the gas curtain achieving the shock

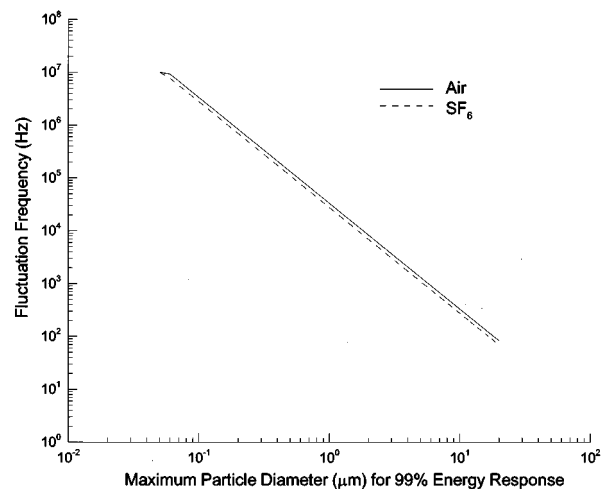


FIG. 3. Maximum particle size for given amplitude fidelity.

piston velocity. The complexity of this situation necessitates considering the response of the fog particles to more complex flowfields than just impulsive acceleration. To analyze the frequency response of a particle exposed to a given frequency of oscillation in the carrier phase, consider writing \mathbf{u}_g and \mathbf{u}_p in (1) in terms of the Fourier integrals

$$\mathbf{v}_p(\omega) = \int_{-\infty}^{\infty} \mathbf{u}_p \exp(-i\omega t) d\omega$$

and

$$\mathbf{v}_g(\omega) = \int_{-\infty}^{\infty} \mathbf{u}_g \exp(-i\omega t) d\omega. \quad (2)$$

The ratio between the energy spectrum of fluctuations of the particulate and the gas, $|\mathbf{v}_p|^2/|\mathbf{v}_g|^2$, at various carrier phase fluctuation frequencies, ω , can be written (Hjelmfelt and Mockros²⁰) as

$$\frac{|\mathbf{v}_p|^2}{|\mathbf{v}_g|^2} = \frac{(18St^2/s)^2}{(18St^2/s)^2 + 1}, \quad (3)$$

where $St = (\nu/\omega d^2)^{1/2}$ is the Stokes number ($\nu = \mu/\rho$ is the carrier phase dynamic viscosity and ω is the fluctuation frequency) and $s = \rho_p/\rho_g$ is the density ratio. An expression for the ratio of the fluctuation amplitudes can also be found.

A maximum acceptable particle size for any given fluctuation frequency in the carrier phase can be determined by requiring that the ratio of the energy spectrum of fluctuations of the particulate be within 1% of those of the gas. Figure 3 shows curves of this maximum diameter for pure water droplets in both air and SF₆. By far, the largest acceleration to be followed by the fog droplets is that following the planar shock wave. A conservative estimate of the entire interaction time of the shock with the gas curtain (compressing and accelerating it) is approximately 10 μ s. This corresponds to a fluctuation frequency of approximately $1/10 \times 10^{-6} \text{ s} = 10^5 \text{ Hz}$. The accelerations associated with the instability flow superimposed on the mean downstream motion are much smaller. A 0.5 μ m particle can successfully

follow such an acceleration as can be seen in Fig. 3. Characterizations of the output of theatrical fog generators¹⁸ have found typical sizes on the order of $0.5\ \mu\text{m}$.

The Weber number, $We = d_p \rho_g U^2 / \sigma$ where U is a characteristic relative velocity and σ is the surface tension, represents the ratio of inertial forces to surface tension confinement. For droplets near $0.5\ \mu\text{m}$, We is small at all times except for possibly a brief period during shock acceleration. Therefore the analysis above considering the droplets as spherical is justified.

In the current shock tube arrangement, all particles able to follow the initial shock impulse with sufficient fidelity will easily track with the subsequent instability flow. In the time interval characteristic of this flow, the influence of diffusion is negligible. Those droplets that cannot follow the initial impulse will quickly become dissociated from the gas curtain and will see little influence of the instability flow. Images produced with the fog tracer closely resemble those relying solely on preferential Rayleigh scattering from SF_6 (Budzinski *et al.*⁵). The images possess clear, small-scale details and thereby give a strong indication of great fidelity of flow tracking by the fog. Although the fog droplets cannot follow the molecular diffusion of the SF_6 into the air, this limitation can only influence the late-time results through processes prior to shock interaction. The flow processes during and after the shock passage take place on time scales much smaller than diffusion times.

An important question associated with the image data produced by this study relates to the correspondence of the intensity data taken to the actual density field in the flow. There are two primary requirements for an accurate depiction of the density field. These are that the fog droplets accurately track the motion of the SF_6 layer and that the initial conditions of intensity and density are similar. The analysis above would indicate good flow tracing by the fog droplets.

The study by Budzinski *et al.*⁵ used the preferential Rayleigh scattering from SF_6 to produce images. These images can be used to determine accurate density fields from the mass fraction of SF_6 and air. Comparison of these data with the light-scattering intensity profiles from fog droplets will help determine the influence of molecular diffusion processes on the initial conditions. Because the droplets cannot follow such diffusion and the post-shock time scales are such that little diffusion can occur, all significant differences should result from different initial conditions. Figure 4 presents intensity profiles from slices through the initial condition exposure in two runs of the same experiment differing only by diagnostic arrangements (i.e. Rayleigh scattering from fog droplets and from SF_6). In each case, three traces are presented from cuts through the thicker regions of the curtain for similar downstream mushroom images. The curves resulting directly from the enhanced scattering (relative to that of air) of the SF_6 depict the trends of the actual density field. Comparison with the intensity profiles of light scattering from fog indicate that, at least initially, the intensity profiles using the fog remain close to the actual density field. If the profile of the initial conditions for the case without fog was determined solely by molecular diffusion (that the fog cannot follow), the initial profiles using the fog

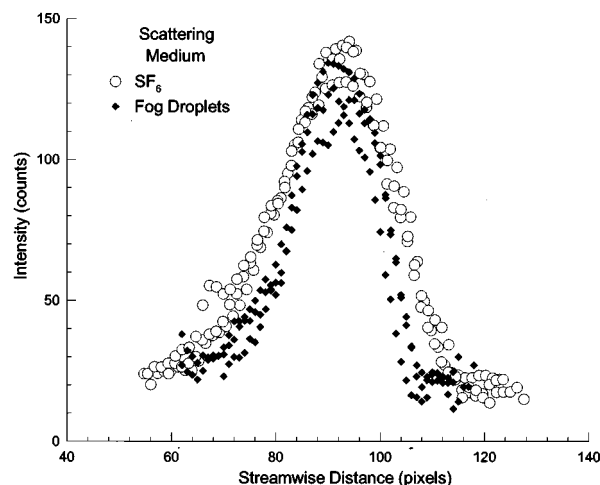


FIG. 4. Pixel intensity profiles at three cross-sections through the gas curtain for SF_6 and fog scattering.

should be narrower (i.e. more of a top-hat profile) than is the case in Fig. 4. Consequently we believe that the fog is an excellent tracer of this flow at both early and late times. However, the possible influence of the fog droplets on the smallest scales of the late-time flow has not been discussed. This does not impact this study directly since we limit our quantitative analysis to the large scales.

III. OBSERVATIONS

A. Gas-curtain morphology

As in the experiments of Jacobs *et al.*,⁴ three main flow patterns were observed: the upstream mushrooms (Fig. 5), the downstream mushrooms (Fig. 6) and the sinuous mode (Fig. 7). All three patterns are characterized by formation of mushroom-shaped features in the perturbed layer, but the orientation of these features and the relative time at which they develop varies. The apparent non-uniform spanwise illumination present in these figures comes from the fact that the laser sheet does not illuminate the entire cross-section of

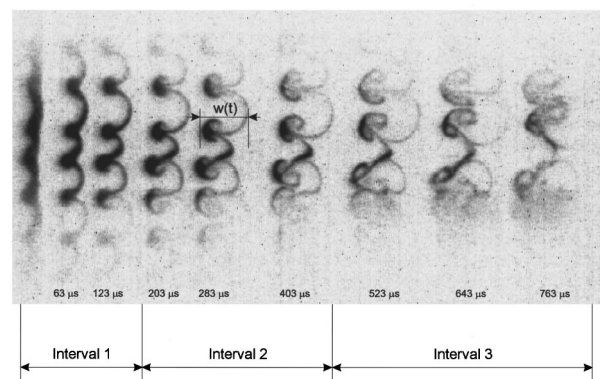


FIG. 5. Upstream mushrooms. Upstream features are narrower than downstream. Three distinct intervals in the evolution of the flow are labeled. As indicated, $w(t)$ is the peak-to-valley width of an individual wavelength of the curtain.

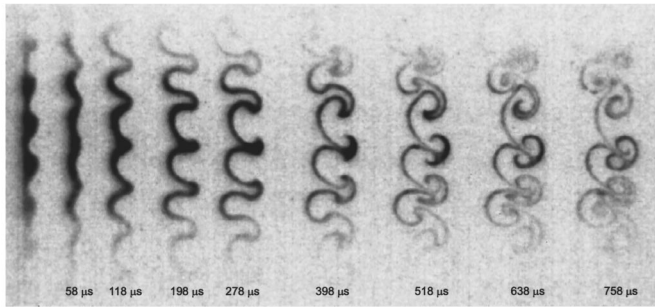


FIG. 6. Downstream mushrooms. Downstream features are narrower than upstream.

the flowfield. The illumination is uniform over the central wavelengths with some spanwise tails of lower intensity.

The upstream mushrooms form quickly after the shock-induced acceleration of the SF_6 layer and develop in the direction opposite to that of the mean translation of the layer. In Fig. 5, one can already see well-formed mushrooms in the third dynamic image of the gas curtain, which corresponds to the time $\sim 200 \mu\text{s}$ after the shock wave hit the layer. The downstream mushrooms, oriented in the direction of the mean layer motion, characteristically take a longer time to emerge. In Fig. 6, mushroom shapes form clearly only at $t \sim 400 \mu\text{s}$ (fifth dynamic image). The initial stages of the evolution of the sinuous mode show the growth of the perturbations of the interface without formation of mushrooms. When mushrooms finally form, their orientation appears to alternate from upstream to downstream, as one can see in the sixth and following dynamic images in Fig. 7 ($t > 500 \mu\text{s}$).

Earlier studies of Budzinski *et al.*⁵ and of Jacobs *et al.*⁴ obtained consistent results regarding the frequency of occurrence of the three late-time flow morphologies with the most frequent being upstream mushrooms. Budzinski *et al.*⁵ correlated the late-time flow structure to the shape of the curtain immediately before shock impact. These studies produced similar frequencies of resulting morphologies by carefully matching the flow rates into and out of the test section and thereby matching the time-varying behavior of the curtain between the studies. The current study did not measure the flow rates associated with the creation of the gas curtain due to the complications associated with the addition of fog. This has resulted in different time-varying characteristics of the laminar curtain and an increased occurrence of late-time downstream mushrooms.

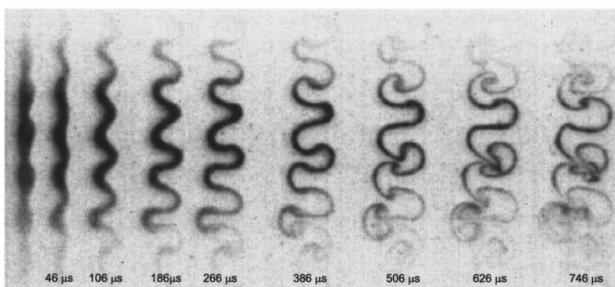


FIG. 7. Sinuous mode. Features are symmetric.

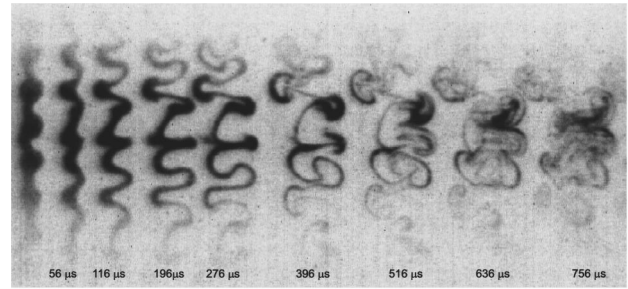


FIG. 8. Coexistence of the three primary flow morphologies.

The high space-time resolution experimental data of the current study confirm that morphology of the interface (upstream mushrooms, downstream mushrooms or sinuous) is determined by the character of the initial perturbations before shock impact, as originally stated by Budzinski *et al.*⁵ If the amplitude of perturbations on the side of the interface oriented toward the shock wave is sufficiently greater than that on the downstream side (Fig. 5), upstream mushrooms form. If both sides of the interface have similar amplitude perturbations and the interface is varicose, a sinuous mode develops (Fig. 7). Finally, if the initial perturbations of the interface are less prominent on the upstream side (mirroring the initial conditions for upstream mushrooms), then downstream mushrooms form (Fig. 6). The initial condition of the gas curtain may contain neighboring wavelengths with differing types of predominant perturbations. In this case, a complex flowfield forms (Fig. 8). Upstream mushrooms, downstream mushrooms and the sinuous mode coexist in the flow. There is little cross-talk visible between the different morphologies in adjacent wavelengths. This differs from earlier studies⁵ where only a single morphology was present for each event. It is also noteworthy that the tail visible on the prominent downstream mushroom in Fig. 8 was first observed in numerical simulations.^{10,15}

There are three temporal intervals present in the evolution of the flow (Fig. 5). The first interval corresponds to the time immediately after the shock wave interaction and is characterized by the roll-up of vorticity deposited by the shock and the growth of the initial perturbation of the layer into a sinuous pattern. The spatial scale prominent in the flow is that of the initial perturbation. The second interval is also vortex dominated and largely deterministic, but structures of smaller spatial scales emerge (e.g. mushroom caps). Finally, during the third interval we observe interaction among neighboring features and growth of structures with scales both smaller and larger than the fundamental. Figure 5 shows the presence of small spatial scales together with the long wavelength perturbation of the gas curtain.

B. Quantification of experimental data

The temporal evolution of the mixing layer formed by the perturbed gas curtain and the surrounding air masses can be characterized by layer thickness w . The initial layer thickness, w_0 , is typically 2 mm after compression. The coexistence of multiple adjacent flow morphologies on one image indicates relatively weak interaction between vortex struc-

tures from one spanwise wavelength to the next. Therefore, data from each wavelength can be analyzed separately. For every image, we measured values $w(t)$ for each spanwise wavelength appearing in the image, with $w(t)$ defined as the distance between the locations of maximum intensity gradients on the upstream and downstream extremes of the layer for a given wavelength.

Plotting the position of the mean displacement of the gas curtain in the dynamic images versus time produces a linear plot, thus making it possible to determine the effective initial moment ($t=0$) by the zero-displacement intercept of the line. The slope of the line corresponds to the shock piston velocity.

A program was written to simplify determining w from the experimental digital photographs. It allowed the user to separate the photograph into strips corresponding to individual wavelengths and measured w for each exposure inside the strip. The program determined the limits of the background pixel values by histogram analysis and searched for vertical boundaries of areas containing non-isolated pixels with pixel values above the maximum background value. In the cases of weak or overlapping images of the gas curtain, the boundaries of the area containing the perturbed curtain were determined manually. For additional validation, curtain widths in one image were measured both with the program and manually. The comparison of the results revealed no systematic differences, with the automatic and manual measurements differing by no more than 2 pixels (0.2 mm in physical space).

There are two possible scenarios of the evolution of w . In the first scenario, the growth of w slows down after $t \sim 400 \mu\text{s}$ and $w(t)$ shows a tendency toward saturation at late times. This kind of evolution could be observed for all three flow patterns and was the dominant type of evolution suggested by other researchers (Jacobs *et al.*⁴). The second scenario, typical only for some upstream mushroom cases, is characterized by $w(t)$ continuing its growth even at late times, without signs of saturation. This type of evolution was not described in earlier works, though it may have been present in the experiments. The current work incorporates the first data sets with adequate temporal resolution to differentiate between the evolution patterns.

Figure 9 shows the measured values of $w(t)$ for upstream mushrooms from six images (from which 24 individual wavelengths are analyzed). For each image considered, w_0 is the mean thickness of the compressed gas curtain in the first dynamic image, immediately after shock interaction. The value of w_0 is computed as the average of w_0 for each of the four individual wavelengths analyzed in the image. Generally, higher values of w_0 lead to higher w at late times. The non-saturating growth is characterized by $w_0 \geq 2 \text{ mm}$.

The behavior of $w(t)$ for the downstream mushrooms and the sinuous mode is similar to that of the saturating upstream mushrooms. Measurements of $w(t)$ for four individual wavelengths from each of three downstream mushroom images and three sinuous mode images are presented in Fig. 10.

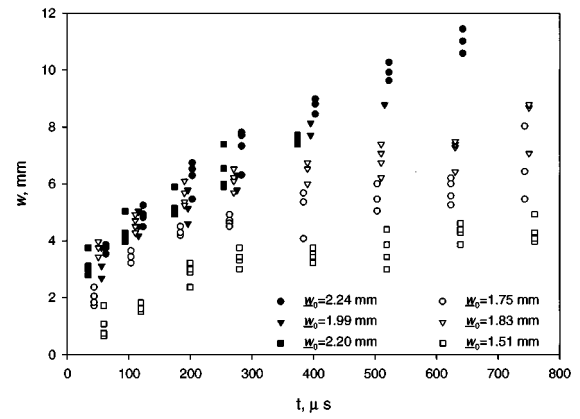


FIG. 9. Mixing layer widths for upstream mushrooms. The filled symbols correspond to data sets with non-saturating growth, the hollow symbols with saturating growth.

IV. ANALYSIS

A. Vorticity production under different initial conditions

Analysis similar to that undertaken by Jacobs *et al.*⁴ helps to establish the relationship between the initial perturbations of the SF_6 layer, vorticity production and the resulting interface morphology. If one considers the two-dimensional vorticity equation (vortex diffusion term dropped),

$$\frac{D}{Dt} \left(\frac{\omega}{\rho} \right) = \frac{1}{\rho^3} \nabla \rho \times \nabla p, \quad (4)$$

it is apparent that the out-of-plane vorticity ω is generated by baroclinic torque at a rate proportional to the cross-product of the pressure and density gradients on the right-hand side of the equation. The dominant pressure gradient in the experiment is that of the shock wave, and the dominant density gradient results from the difference between the densities of air and SF_6 at the interfaces of the gas curtain.

Thus most vorticity is produced in the areas where the boundary of the mixing layer is at the maximum angle with respect to the incident shock wave. Figure 11 illustrates the

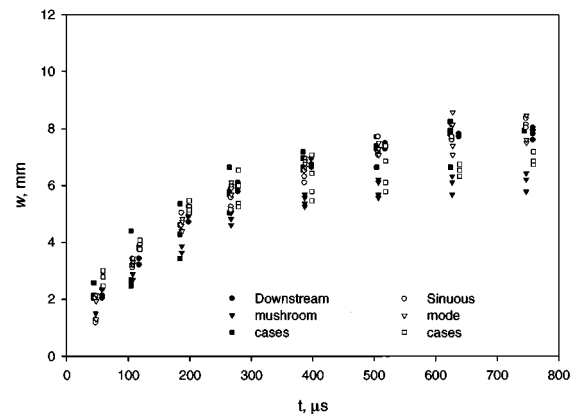


FIG. 10. Mixing layer widths for downstream mushrooms and sinuous mode. The growth is saturated.

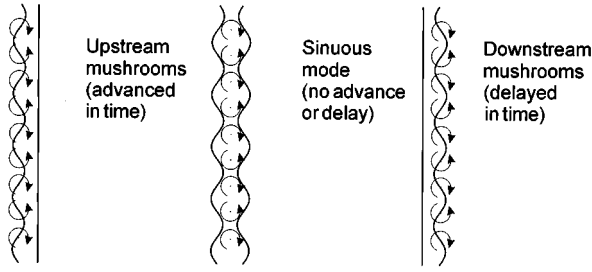


FIG. 11. Vorticity generation under different initial conditions. The subsequent morphology depends on the relative position of the gas curtain and the vortices.

simplified concept of vorticity generation. In the case of a symmetric varicose layer considered by Jacobs *et al.*,⁴ vorticity of the same sign produced on either side of the gas curtain merges to form a row of diffuse vortices with alternating sign and spacing equal to half the wavelength of the initial perturbation. In the case when the initial conditions are not symmetric and only one side of the curtain is perturbed, essentially all of the vorticity is deposited on the perturbed side of the layer. In the case when the upstream side of the curtain is perturbed, the shock propagates from lower-density gas to higher-density gas and the initial perturbation starts to grow in amplitude instantly. The perturbation of the downstream side (where the shock propagates from heavy gas into light gas) alone first has to undergo a phase inversion. This perspective explains the more rapid growth of the upstream mushrooms observed in experiment. It also clarifies why the vortex-like structures appear at relatively late times in the sinuous mode.

B. Vortex-blob simulation

To what extent does the vortex structure deposited by the interaction of the gas curtain with the shock wave govern the evolution of the gas curtain? A simple numerical model has been constructed to simulate the evolution of the gas curtain after the interaction with the shock wave is over and the row of the vortices is formed. It is based on the vortex-blob method described in detail by Nakamura *et al.*²¹ The vorticity field formed in the process of interaction of the shock wave with the gas curtain is assumed to have the form of an infinite row of vortex cores of strength Γ with alternating sign located at coordinates \mathbf{r}_j :

$$\mathbf{r}_j = (\pi k j, 0), \quad \Gamma_j = (-1)^{|j|} \Gamma, \quad j = 0, \pm 1, \pm 2, \dots \quad (5)$$

Here $k = 2\pi/\lambda$ denotes the wave number of the initial perturbation. The distribution of vorticity within each vortex core, characterized by radius δ , is assumed to be Gaussian:

$$g(|\mathbf{r} - \mathbf{r}_j|/\delta) = 1 - \exp(-|\mathbf{r} - \mathbf{r}_j|^2/\delta^2), \quad (6)$$

where $g(y)$ is the circulation contained within radius y . With the ideal, linear initial distribution of the vortex cores as described, their positions do not change with time due to symmetry. Visualization of the simulation (Fig. 12) was done as follows. To account for the initial condition of the gas curtain, at the moment $t=0$, 4710 marker particles are

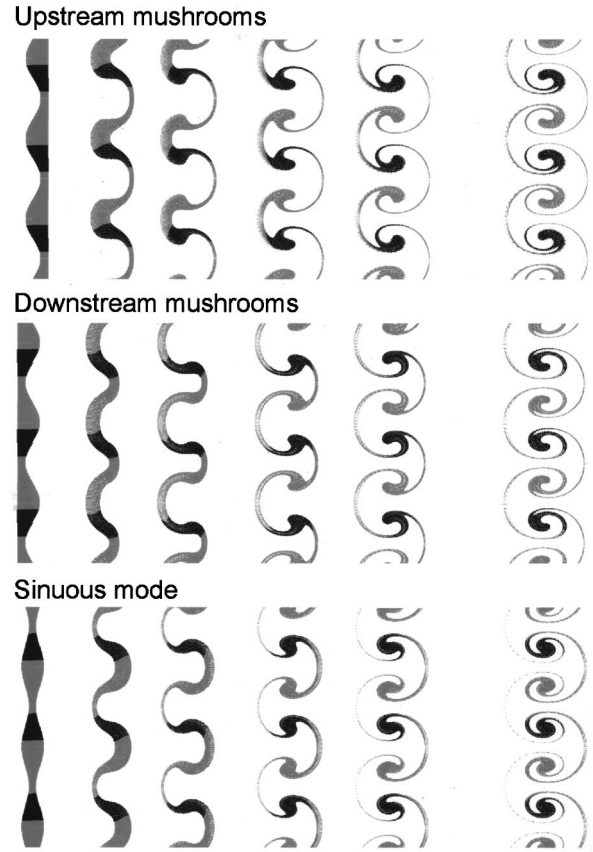


FIG. 12. Vortex-blob simulation of possible flow morphologies.

inserted into the velocity field generated by the row of the vortices. The particles are evenly distributed across one wavelength $\lambda = 6.28$ mm between the boundaries y_u (upstream) and y_d (downstream), defined as (in mm)

$$y_u = 0.6 \sin(x) \quad \text{and} \quad y_d = 1.2 \quad (7)$$

for the upstream mushroom simulation,

$$y_u = -1.2 \quad \text{and} \quad y_d = -0.6 \sin(x) \quad (8)$$

for the downstream mushroom simulation and

$$y_u = -0.3 \sin(x - 0.6) \quad \text{and} \quad y_d = 0.3 \sin(x + 0.6) \quad (9)$$

for the sinuous case. The core radius δ can be varied from 0 to 1.5 mm, the vortex strength Γ is set at the value 0.03.

The model is deliberately simple. To isolate the influence of the initial vorticity distribution on the structure of the flow, it does not explicitly account for the effects of density gradients, diffusion or compressibility. The velocity field due to the row of vortex blobs does not change in time and is the same for all the simulations. Only the initial positions of the marker particles change with respect to the vortex row. Figure 12 shows the visualization of the movement of marker particles for all three types of the initial conditions with $\delta = 1.2$ mm and $\Gamma = 0.03$. The timing intervals and spacing between the consecutive images were selected to match those of the experimental photographs. Early evolution of the simulated patterns is remarkably similar to the experiment. At later times, the simulated curtain retains its symmetry, which is not the case for the experimental images. This com-

parison suggests that the difference in the streamwise position of the shock-induced vortices with respect to the gas curtain interfaces produces the initial differentiation of the flow morphologies.

C. Point vortex model as the basis for curve-fitting

For each wavelength, some quantitative properties, such as the initial compressed thickness w_0 , thickness $w(t)$ and the local wave number $k=2\pi/\lambda$ can be measured or estimated from the image data. An important flow characteristic that cannot be measured directly is the circulation Γ of the vortices that form due to interaction of the shock wave with the curtain.

The apparent correspondence of the actual gas-curtain evolution in the experimental photographs with the evolution of the layer of the marker particles in the simplified vortex-blob model (Fig. 12) suggests the use of the point vortex row model described by Jacobs *et al.*⁴ to analyze the experimental $w(t)$ curves. This model produces an expression for the growth of the thickness w of the gas curtain under the influence of an infinite number of counterrotating vortices:

$$w(t) = \frac{2}{k} \sinh^{-1} \left(k^2 \Gamma t + \sinh \left(\frac{k w_0}{2} \right) \right). \quad (10)$$

The initial curtain width, w_0 , in Eq. (10) corresponds to the width of the curtain *after* it has been compressed by the shock wave, so it can be estimated as the width of the pre-shock initial condition of the curtain (obtained from the digital photographs) divided by the shock compression ratio. Thus the obvious choice for the free parameter of a one-parameter fit should be Γ . The fit can be differentiated to determine the growth rate dw/dt .

It is important to keep in mind that the idealized point vortex model does not account for many significant features present within the experimental flowfield. First, the interaction of the shock wave with the heavy gas curtain does not produce a row of vortex points. Instead, the interaction produces a distributed, sinusoidally varying field of vorticity. During the early time, while concentrations of vorticity of the same sign form from the initial distribution, the point vortex model is inapplicable. Second, the vortex cores that form are of finite size. Third, the width values predicted by the model are valid only for the perfect sinuous mode growth. The model can neither predict the relative time advance associated with upstream mushrooms, nor the time delay associated with the downstream mushrooms. The latter delay adds to the time interval associated with vorticity accumulation and arises from the phase inversion characteristic of the downstream mushroom morphology. In the downstream mushroom case, the phase inversion moves $w(t)$ through a local *minimum* which the monotonically increasing model is unable to predict. Finally, irregularities and violations of periodicity within the initial conditions of the gas curtain result in non-uniformities both in the spacing and strength of the vortex cores. Nevertheless, this model is a useful approximation and serves well as a physics-based fitting function.

Figure 13 shows values of $w(t)$ obtained by numerical

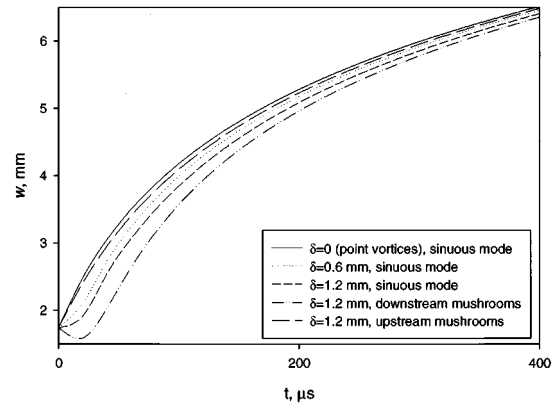


FIG. 13. Vortex-blob model—influence of core radius δ and initial conditions.

simulation as described in the previous subsection. The increase of the characteristic core size δ produces delay in the growth of $w(t)$. The delay in the development of the downstream mushrooms due to the phase inversion of the interface and the presence of the local minimum in the downstream mushroom case are also apparent. Correspondingly, the growth of upstream mushrooms is characterized by time advancement when compared with the sinuous case.

D. Curve-fitting

Due to the importance of the baroclinic torque represented in Eq. (4), the vorticity (and therefore the circulation) present within the flowfield is an important quantity in the evolution of the instability flow. Comparison of the measured data to simplified models such as that presented in Eq. (10) not only suggests the extent to which the instability flow is due to vortical motions, but also enables the estimation of circulation values without requiring direct measurements of the velocity field. Such estimates are of great interest in the benchmarking of codes relating to such instability flows. Finally, the fitting of the experimental data to a physical model allows the estimation of the growth rate (through the differentiation of the model), which is another quantity of interest in current studies of the Richtmyer–Meshkov instability.

We used commercial curve-fitting software²² to process the tables of experimental values $w(t)$. The curve-fitting scheme implemented in the software is based on the least squares algorithm. For our data sets, the curve-fitting goal was set to minimization of the sum of residual squares

$$SS = \sum_{i=1}^n (w_i - \hat{w}_i)^2, \quad (11)$$

where w_i denotes the experimental value and \hat{w}_i the corresponding value retrieved from Eq. (10). The error of the resulting fit χ was measured as

$$\chi = \sqrt{\frac{1}{n-1} \sum_{i=1}^n (w_i - \hat{w}_i)^2}. \quad (12)$$

The compression factor for the shock wave of $M=1.2$ was calculated to be 1.342, so the value of w_0 was estimated

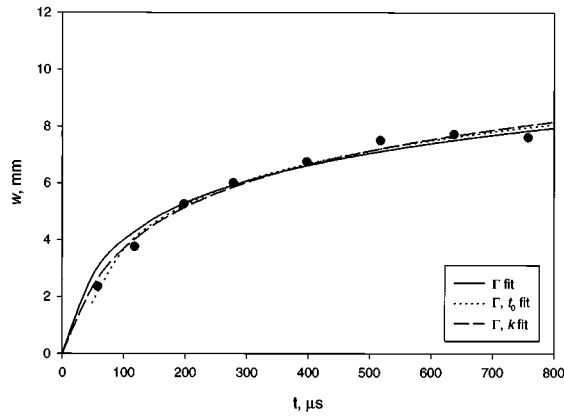


FIG. 14. Curve-fit—downstream mushrooms.

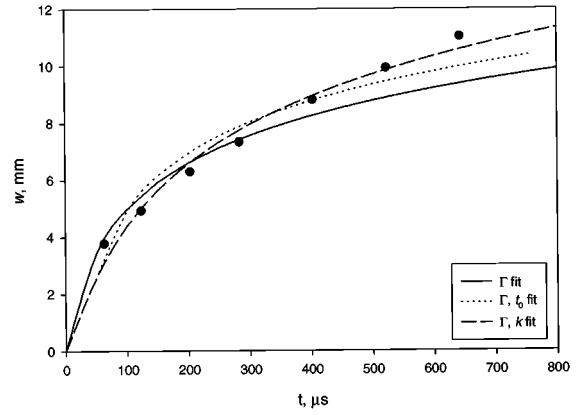


FIG. 16. Curve-fit—upstream mushrooms.

from the thickness of the gas curtain before shock acceleration w_{init} as $w_0 = w_{init}/1.342$. For an alternative estimate of w_0 , the area occupied by the compressed gas curtain per wavelength in the first exposure after the shock can be measured and divided by the wavelength. The results yielded by these methods agree well (within 5%).

Within each class of flow morphology (saturating upstream mushrooms, non-saturating upstream mushrooms, downstream mushrooms, sinuous mode) the results of curve-fitting are similar. Figures 14, 15 and 16 show curve fits for $w(t)$ corresponding to one spanwise wavelength of the flow patterns in Figs. 5, 6 and 7.

Curve-fitting with Γ as the only free parameter, suggested in the previous subsection, produces fits that persistently over-predict $w(t)$ at early times ($t \lesssim 250 \mu s$) and under-predict it at later times. The resulting values of error χ vary from 0.6 to 1.4 in the downstream mushroom and sinuous mode data sets that were analyzed, when w_0 is set to the value estimated from the experiment. It is noteworthy that setting $w_0 = 0$ reduces the error χ to the levels between 0.3 and 0.6, though the tendency to over- and under-prediction remains and in many cases the single-parameter fit misses the curvature of the experimental data profile completely. For the non-saturating upstream mushrooms, the value of χ characterizing the one-parameter fit exceeds 1. The fitted value of Γ is unlikely to be reliable, because the fit

produces large errors and misses the curvature of the data. Also, the one-parameter fit should not be used in estimating growth rates through differentiation, as it produces a systematic error.

To improve the quality of the fit, we considered two-parameter fits with the curve-fitting schemes constructed to account for the physical flow features not present in the initial model. To make the curve-fitting algorithm “sense” the time shift due to the vortex core size, phase inversion-related effects due to the asymmetry in the initial conditions and the vortex roll-up delay, we consider time in the form $t - t_0$, where t_0 represents the shift (positive or negative) due to all the influences mentioned in the previous two paragraphs. Then Eq. (10) assumes the form

$$w(t) = \frac{2}{k} \sinh^{-1} \left(k^2 \Gamma (t - t_0) + \sinh \left(\frac{k w_0}{2} \right) \right), \quad (13)$$

and a two-parameter fit (Γ, t_0) is obtained. The parameter t_0 is dependent on the value of w_0 in this scheme, as the terms containing these two values in Eq. (13) can be separated from the term involving the independent variable t . However, with w_0 estimated from the experimental data, the values of t_0 retrieved by this fit should be consistent with the observed flow morphology—greatest for downstream mush-

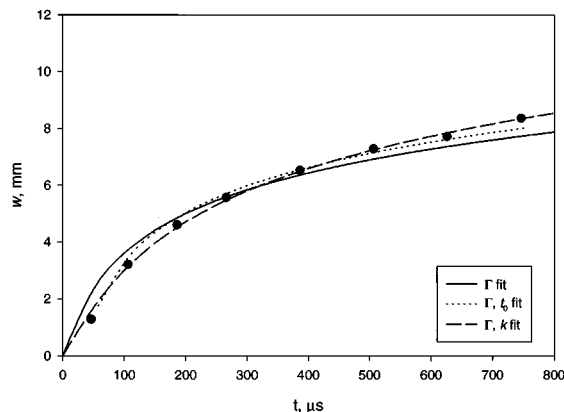


FIG. 15. Curve-fit—sinuous mode.

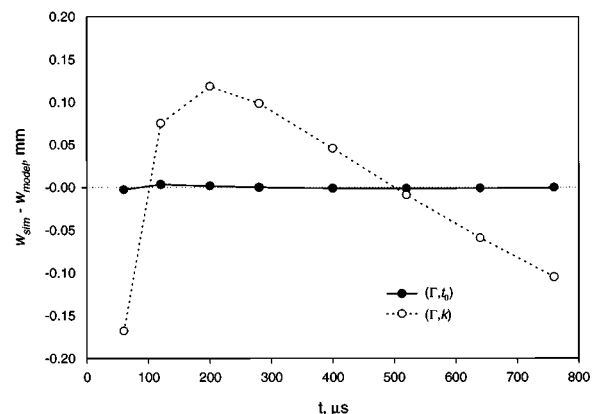


FIG. 17. Results of curve-fitting $w(t)$ data from vortex-blob simulation of upstream mushroom pattern.

TABLE I. Results of curve-fitting $w(t)$ data from vortex-blob simulation.

Simulated downstream mushrooms ($\Gamma=0.03, k=1$)					
Curve fit	w_0 mm	Γ	k mm^{-1}	t_0 10^{-6} s	χ
Γ, t_0	1.74	0.030	1.00	35.6	0.006
Γ, k	0.00	0.029	0.98	0.00	0.012
Simulated upstream mushrooms ($\Gamma=0.03, k=1$)					
Curve fit	w_0 mm	Γ	k mm^{-1}	t_0 10^{-6} s	χ
Γ, t_0	1.74	0.030	1.00	-14.9	0.002
Γ, k	0.00	0.050	1.25	0.00	0.103

rooms, smaller for the sinuous mode and the smallest for upstream mushrooms. This feature can be used as an extra consistency check, and can be used to quantitatively categorize any given $w(t)$ curve.

The second two-parameter fitting scheme can be suggested by the following. In the model, k is the spacing along the infinite row of vortex points of equal strength. The inter-vortex spacing on the images is not uniform (as appears to be the case of the vortex strengths as well) and this spacing changes with time (e.g. Fig. 5). The digital images do not portray the locations of vortices (rather, only the influence of these vortical structures on the gas curtain) except at late time (when there are well-defined ‘‘vortex cores’’ flanking the mushrooms). An estimate of the spacing can be obtained from the local wavelength at the initial conditions. Therefore, due to the fact that the wave number appearing in the model can change with time and can only be estimated from the images except at very late time, it is difficult to determine the ‘‘correct’’ value of k for any particular wavelength from the experimental data. Using k as a parameter produces the (Γ, k) fit.

A few notes related to the general properties of the (Γ, k) and (Γ, t_0) fits remain to be made before the discussion of the results obtained by curve-fitting different sets of the experimental data.

First, the sensitivity of w to the fitting parameters as $t \rightarrow +\infty$ must be considered. If $w(t)$ is taken in the form (13), the following expressions for the limits are valid:

$$\frac{\partial w}{\partial k} \rightarrow \infty, \quad t \rightarrow \infty, \quad (14)$$

$$\frac{\partial w}{\partial t_0} \rightarrow 0, \quad t \rightarrow \infty, \quad (15)$$

TABLE II. Results of curve-fitting experimental $w(t)$ data: upstream mushrooms.

Curve fit	w_0 mm	Γ	k mm^{-1}	t_0 10^{-6} s	χ
Γ	0.00	0.056	0.84	0.00	1.05
Γ, t_0	2.79	0.076	0.84	54.1	0.67
Γ, k	0.00	0.049	0.57	0.00	0.34

$$\frac{\partial w}{\partial \Gamma} \rightarrow 2/k\Gamma, \quad t \rightarrow \infty. \quad (16)$$

Thus there exists a potential for the (Γ, k) fit to be over-sensitive to k at late times.

Second, it is instructive to apply the two-parameter curve-fitting schemes based on the point-vortex model to simulated $w(t)$ plots generated by the vortex-blob code and to check for the presence of systematic errors in $(w_i - \hat{w}_i)$ and in the values of Γ estimated from the fitting. Figure 17 shows the residual $(w_i - \hat{w}_i)$ values for the simulated upstream mushrooms morphology with the initial conditions as described in Section IV B and with $\delta = 1.2$ mm. Time intervals between the data points were set to imitate the timing of exposures in the experiment. Uniform weighting was used. A weighting scheme with the first point skipped might be beneficial for the downstream mushroom cases if the first measured dynamic value of $w(t)$ corresponds to the non-monotonic interval of the w evolution due to phase inversion. The (Γ, t_0) fits are sensitive to the weighting of the first point when estimate values of t_0 are positive and large.

As one can see in Fig. 17, the (Γ, k) fits produce a considerable systematic error. The influence of loading the middle of the weighting distribution leads mostly to shifting the residual plots up and down without changing their character, so in curve-fitting the experimental data we used only uniform weighting. The (Γ, t_0) fits produce a much smaller error and are less sensitive to different weightings. The same tendencies can be observed for the simulations of the sinuous mode and downstream mushrooms with non-zero values of δ . For the latter, curve-fitting (Γ, k) with $w_0 = 0$, though non-physical, produces a somewhat better fit. This can be explained by the fact that letting w ‘‘grow’’ from zero rather than from its actual initial value introduces a delay similar to that created by adding t_0 . Thus we set w_0 to zero in the (Γ, k) fits applied to experimental data.

Table I shows the values of parameters used in and retrieved by curve-fitting the simulated data for the upstream and downstream mushrooms. The (Γ, t_0) fit produces very good results in terms of χ , and the values of t_0 for the upstream and downstream mushrooms are respectively negative and positive. The error is reasonably small for the (Γ, k) fit with $w_0 = 0$ in the downstream mushroom case, and for the (Γ, k) fit with $w_0 = 1.74$ mm in the upstream mushroom case, but in neither case do the (Γ, k) fits retrieve accurate values of Γ and k . As the initial conditions and the values of δ vary, the (Γ, k) fit can both over- and under-predict Γ and k . The error in Γ can be as great as 33%, and the small value of χ alone does not guarantee the accuracy of Γ produced by the (Γ, k) fit.

Figure 14 illustrates the results of curve-fitting the non-saturating upstream mushroom data with uniformly-weighted one- and two-parameter fits. The values of Γ , t_0 , k and χ for this fit are in Table II. This data set is characterized by considerable asymmetry in the position of vortices, and the (Γ, k) fit produces the best results in terms of error ($\chi = 0.34$). The slope of the curve-fit does not represent the trend in the actual experimental data. The mismatch in the values of Γ

TABLE III. Results of curve-fitting experimental $w(t)$ data: downstream mushrooms.

Curve fit	w_0 mm	Γ	k mm^{-1}	t_0 10^{-6} s	χ
Γ	0.00	0.033	1.05	0.00	0.38
Γ, t_0	1.78	0.040	1.05	48.2	0.22
Γ, k	0.00	0.031	0.92	0.00	0.26

estimated by the two-parameter fits is rather high ($\sim 40\%$), which can indicate a poor reliability of the Γ estimate in this particular case. As was mentioned before, results for curve-fitting other wavelengths in the data set and in other data sets with the same morphology (non-saturating upstream mushrooms) are similar. It is also important to note that the results of curve-fitting *saturating* upstream mushrooms produce much lower values of χ and better fits.

The non-saturating upstream mushroom experimental images typically show mode coupling and the emergence of wavelengths longer than the wavelength of the initial perturbation. Interaction between individual wavelengths in the gas curtain is likely to limit the applicability of the point-vortex formulas for curve-fitting this particular pattern of evolution.

In the case of the downstream mushrooms (Fig. 15 and Table III), the one-parameter curve-fit does exhibit the characteristic over- and under-prediction of w , though the error is relatively low ($\chi=0.38$). Both of the two-parameter fits (uniform weighting) follow the trends in the experimental data quite well, with the (Γ, t_0) fit producing a slightly lower error $\chi=0.22$ versus $\chi=0.26$ for the (Γ, k) fit. The value of k retrieved by this fit is close to that estimated from experimental data -0.92 mm^{-1} versus 1.05 mm^{-1} . The Γ values produced by (Γ, k) and (Γ, t_0) fits are also consistent, differing only by about 20%.

The sinuous mode cases (Fig. 15 and Table IV) are also typically characterized by reasonable agreement between the (Γ, k) and (Γ, t_0) fits. The (Γ, k) fits often follow the general trend in the evolution of data more accurately and thus would be preferable for instability growth-rate estimation. As the analysis of the vortex-blob simulated data shows, more reliable values of Γ are likely to be estimated by the (Γ, t_0) fits.

The fits can be differentiated with respect to time to provide estimates for the instability growth rates. Figure 18 shows dw/dt for the (Γ, k) fits in Figs. 14, 15 and 16. The first $100 \mu\text{s}$ are not shown in this figure as the model cannot account for initial non-monotonic growth due to phase inversion in the case of downstream mushrooms. The curves depict saturation growth rates. For the upstream mushroom image, saturation is an artifact of the model which cannot

TABLE IV. Results of curve-fitting experimental $w(t)$ data: sinuous mode.

Curve fit	w_0 mm	Γ	k mm^{-1}	t_0 10^{-6} s	χ
Γ	0.00	0.030	0.96	0.00	0.51
Γ, t_0	1.76	0.035	0.96	57.8	0.21
Γ, k	0.00	0.026	0.70	0.00	0.14

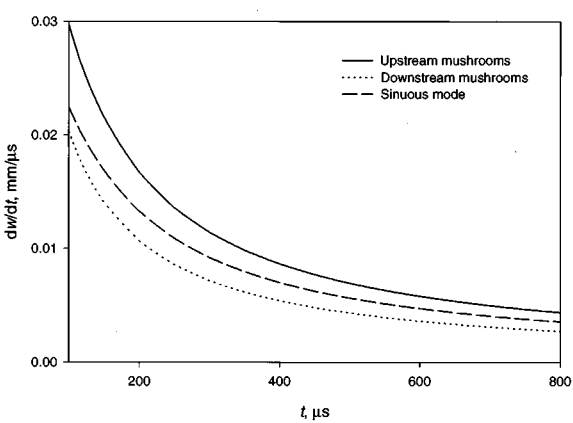


FIG. 18. Growth rates $dw(t)/dt$ for Γ, k curve-fits. The downstream mushroom exhibit the greatest delay, the sinuous mode grows faster and the upstream mushrooms are the fastest.

produce non-saturating growth rates. These saturation growth rates are similar in magnitude and shape to those from analysis of the single-interface Richtmyer–Meshkov instability.¹⁶ The early-time behavior of the growth rates cannot be determined in this study due to limitations on the temporal resolution of the data imposed by the experimental conditions and diagnostics. The relative time shifts due to phase inversion for each of the three flow morphologies distinguish the growth-rate curves.

Several curve-fits using Eq. (10) or its forms and containing more than two free parameters were also examined, but they demonstrated strong parameter dependency and thus were disregarded as over-parametrized.

Using combinations of more than two varying parameters was found to over-parametrize the system, suggesting only two truly independent variables. The best fit (in terms of the error χ) was actually produced by a fourth-order polynomial. Such a fit may also be useful in the computation of growth rates.

V. CONCLUSIONS

For the first time experimental data are generated to record the time history of the evolution of a shock-accelerated heavy-gas curtain with sufficient spatial and temporal resolution to observe the formation of different instability morphologies and their development into a state of mode coupling and incipient turbulence. The three, distinct late-time flow morphologies (i.e. downstream mushrooms, upstream mushrooms and the sinuous mode) seen in previous experiments are reproduced. However, some laser-sheet images now show the coexistence of two or three of these morphologies during a single event. The development of the instability from the initial perturbation is quantified in terms of the total mixing layer width $w(t)$, providing a set of benchmarks for large-scale numerical simulations designed for highly distorted flows. Our simple simulations employing a vortex-blob model generate morphologies closely resembling those observed experimentally, thus providing visual

confirmation that the flow is vortex dominated after the initial acceleration induces Richtmyer–Meshkov instability and consequent vortex roll-up.

Analysis of the experimental data with curve-fits based on the analytical expressions for the flow generated by a row of point vortices produced consistent estimates of the shock-induced circulation in the experiment. For the upstream mushroom morphology, two distinct evolution patterns were observed. In the case of moderately perturbed initial conditions, the growth of the mixing layer width reaches saturation as in the case of both downstream mushrooms and the sinuous modes. In the case of a more severe initial perturbation, no saturation is observed within the time interval recorded in the experiments. This latter pattern is also characterized by mode coupling and other indications of pre-turbulent behavior.

These experimental observations are based on an innovative diagnostic system using cooled fog as a tracer, a pulsed laser and gated CCD camera. The combination of this laser-sheet technique and analysis with two simple models enables estimation of the shock-induced vorticity field without direct measurement of the velocity field.

ACKNOWLEDGMENTS

We are grateful to Frank Kosel and Hadland Photonics, Ltd. for use of the SVR camera, to Lynn Veaser, Doug Fulton and Dave Oro for use of the Nd:YLF laser, and to Chris Gossein for technical assistance. We would like to acknowledge useful discussions with Frank Harlow, Charles Cranfill and Ryan Martin. This work was performed under U.S. Department of Energy Contract No. W-7405-ENG-36.

¹R. D. Richtmyer, "Taylor instability in shock acceleration of compressible fluids," *Commun. Pure Appl. Math.* **23**, 297 (1960).

²E. E. Meshkov, "Instability of the interface of two gases accelerated by a shock wave," *Izv. Akad. Nauk. SSSR Mekh. Zhidk. Gaza* **4**, 151 (1969). [Russian: *Izv. Acad. Sci. USSR Fluid Dyn.* **4**, 101 (1969)].

³J. W. Jacobs, D. L. Klein, D. G. Jenkins, and R. F. Benjamin, "Instability growth patterns of a shock-accelerated thin fluid layer," *Phys. Rev. Lett.* **70**, 583 (1993).

⁴J. W. Jacobs, D. G. Jenkins, D. L. Klein, and R. F. Benjamin, "Nonlinear growth of the shock-accelerated instability of a thin fluid layer," *J. Fluid Mech.* **295**, 23 (1995).

⁵J. M. Budzinski, R. F. Benjamin, and J. W. Jacobs, "Influence of initial conditions on the flow patterns of a shock-accelerated thin fluid layer," *Phys. Fluids* **6**, 3510 (1994).

⁶G. H. McCall, "Laser-driven implosion experiments," *Plasma Phys.* **25**, 237 (1983).

⁷A. Burrows, J. Hayes, and B. A. Fryxell, "On the nature of core-collapse supernova explosions," *Astrophys. J.* **450**, 830 (1995).

⁸J. M. Stone, J. Xu, and L. G. Mundy, "Formation of 'bullets' by hydrodynamical instabilities in stellar outflows," *Nature (London)* **377**, 315 (1995).

⁹B.-I. Jun and T. W. Jones, "Interaction of Rayleigh–Taylor fingers and circumstellar cloudlets in young supernova remnants," *Astrophys. J.* **468**, L59 (1996).

¹⁰R. M. Baltrusaitis, M. L. Gittings, R. P. Weaver, R. F. Benjamin, and J. M. Budzinski, "Simulation of shock-generated instabilities," *Phys. Fluids* **8**, 2471 (1996).

¹¹D. C. Besnard, F. H. Harlow, R. M. Rauenzahn, and C. Zemach, "Spectral transport model for turbulence," *Theoret. Comput. Fluid Dynam.* **8**, 1 (1996).

¹²C. W. Cranfill, "A new multifluid turbulent mix model," Los Alamos Report LA-UR-92-2484 (1992).

¹³D. M. Snider and M. S. Andrews, "Rayleigh–Taylor and shear driven mixing with an unstable thermal stratification," *Phys. Fluids* **6**, 3324 (1994).

¹⁴G. L. Brown and A. Roshko, "On density effects and large structure in turbulent mixing layers," *J. Fluid Mech.* **64**, 775 (1974).

¹⁵K. O. Mikaelian, "Rayleigh–Taylor and Richtmyer–Meshkov instabilities in finite-thickness fluid layers," *Phys. Fluids* **7**, 888 (1995).

¹⁶J. W. Grove, R. Holmes, D. H. Sharp, Y. Yang, and Q. Zhang, "Quantitative theory of Richtmyer–Meshkov instability," *Phys. Rev. Lett.* **71**, 3473 (1993).

¹⁷The fog generator used was a "Fog Hog" using "Euro Fog Fluid" both of which are manufactured by the American DJ Company, Hollywood, CA.

¹⁸Entertainment Services & Technology Association, "Introduction to Modern Atmospheric Effects" (1996).

¹⁹P. M. Rightley and R. F. Benjamin, "High-speed flow visualization of fluid instabilities," 22nd International Congress on High-Speed Photography and Photonics (1996).

²⁰A. T. Hjelmfelt and L. F. Mockros, "Motion of discrete particles in a turbulent fluid," *Appl. Sci. Res.* **16**, 149 (1966).

²¹Y. Nakamura, A. Leonard, and P. R. Spalart, "Vortex simulation of an inviscid shear layer," AIAA-82-0948, AIAA/ASME 3rd Joint Thermophysics, Fluids and Heat Transfer Conference (1982).

²²SigmaPlot v. 3.03 by Jandel Scientific Corporation, San Rafael, CA.